Nanoscale

PAPER

View Article Online
View Journal | View Issue

Cite this: *Nanoscale*, 2024, **16**, 10597

Ferroelectric field enhanced tribocatalytic hydrogen production and RhB dye degradation by tungsten bronze ferroelectrics†

Zhihong Zhu,[a] Zuheng Jin,[a] Chuan Jiang,[a] Sha Wu,[a] Changzheng Hu, *[a,b] Laijun Liu, [a,b] Liang Fang[a,b] and Zhenxiang Cheng *[c]

Received 29th February 2024,
Accepted 17th April 2024

DOI: 10.1039/d4nr00868e

rsc.li/nanoscale

Tribocatalysis is a method that converts mechanical energy into chemical energy. In this study, we synthesized tungsten bronze structured $Ba_{0.75}Sr_{0.25}Nb_{1.9}Ta_{0.1}O_6$ ferroelectric ceramic submicron powder using a traditional solid-state route, and the powder exhibited excellent performance in tribocatalytic water splitting for hydrogen production. Under the friction stirring of three polytetrafluoroethylene (PTFE) magnetic stirring bars in pure water, the rate of hydrogen generation by the $Ba_{0.75}Sr_{0.25}Nb_{1.9}Ta_{0.1}O_6$ ferroelectric submicron powder is 200 μmol h^{-1} g^{-1}, and after 72 hours, the accumulated hydrogen production reaches 15 892.8 μmol g^{-1}. Additionally, this ferroelectric tungsten bronze ferroelectric material also exhibits excellent tribocatalytic degradation ability toward RhB dyes, with degradation efficiency reaching 96% in 2 hours. The study of tribocatalysis based on tungsten bronze ferroelectric materials represents a significant step forward in versatile energy utilization for clean energy and environmental wastewater degradation.

1. Introduction

With the continuous advancement of human society, the demand for energy is on the rise.[1,2] Currently, the most vital fossil energy sources are dwindling, and the emission of substantial amounts of greenhouse gases poses severe global environmental issues.[3,4] As a response, new clean and renewable energy sources remain a point of interest.[5] Hydrogen, as a new form of energy that can be generated by splitting water, is gaining popularity due to its eco-friendliness and the potential for reuse.[6] Photocatalytic hydrogen generation is a process that converts water into hydrogen and oxygen by photo-excited electron–hole pairs, offering benefits such as eco-friendliness and simplicity, and has been extensively researched.[7–11] Furthermore, various other catalytic hydrogen production techniques have been extensively documented, such as piezoelectric catalysis,[12,13] pyroelectric catalysis,[14] and electrocatalysis.[15] Nevertheless, certain constraints hinder the practical application of photocatalytic hydrogen generation, such as low solar energy utilization rates and stringent environmental conditions.[16,17] Piezoelectric catalysis necessitates high-frequency ultrasonic vibration to attain reaction conditions, making it challenging to implement in natural settings. Electrocatalytic hydrogen generation is currently the predominant industrial approach for producing hydrogen; however, its high cost and limited precision control present significant challenges.[18] Consequently, the development of an innovative catalyst for hydrogen generation is particularly essential.

Tribocatalysis, as a method for converting mechanical energy into chemical energy, has been proven to be an effective means of utilizing mechanical energy.[19–21] In recent years, friction energy has been increasingly utilized in the field of catalysis, leading to numerous reports on the degradation of dyes by tribocatalysis, using $Ba_{0.75}Sr_{0.25}TiO_3$,[22] Bi_2WO_6,[23] $Bi_{12}TiO_{20}$,[24] and FeS_2.[25] In comparison with other materials, polytetrafluoroethylene (PTFE) exhibits facile electron access during friction, outstanding temperature adaptability, chemical inertness, resilience to strong acids and bases, and exceptional aging resistance.[26,27] Consequently, PTFE magnetic stirring bars are frequently utilized in friction catalysis investigations. Furthermore, some researchers found that water could be split by PTFE magnetic stirring of various oxides as early as two decades ago.[28–30] In recent years, Li *et al.* demonstrated the production of combustible gases through friction-induced TiO_2 oxidation.[31] Furthermore, some researchers have

[a]*Key Laboratory of Nonferrous Metal Oxide Electronic Functional Materials and Devices, Education Department of Guangxi, College of Materials Science and Engineering, Guilin University of Technology, Guilin 541004, China.*
E-mail: huchzh@foxmail.com; Tel: +86-773-5896290
[b]*Collaborative Innovation Centre for Exploration of Nonferrous Metal Deposits and Efficient Utilization of Resources in Guangxi, Guangxi Key Laboratory of Optical and Electronic Materials and Devices, Guilin University of Technology, Guilin, 541004, China*
[c]*Institute for Superconducting and Electronic Materials, University of Wollongong, Innovation Campus, Squires Way, North Wollongong, NSW 2500, Australia.*
E-mail: cheng@uow.edu.au; Tel: +61-2-42981406

† Electronic supplementary information (ESI) available. See DOI: https://doi.org/10.1039/d4nr00868e

utilized copper friction to convert H_2O and CO_2 into combustible gases in water.[32] These studies have indicated that tribocatalysis has strong potential for hydrogen production.

Tungsten bronze structured ferroelectric materials exhibit remarkable structural tunability and flexibility, which can be attributed to their intricate structure and the diverse ionic positions within the unit cell.[33] And they also have the capability to effectively promote carrier migration due to their spontaneous polarization. This property can enhance the separation efficiency of electrons and holes and play a crucial role in catalysis.[34,35] Tungsten bronze materials have been employed for various catalytic applications in recent years.[36–38] Additionally, Yoshizawa utilized tungsten bronze structured $Sr_2KTa_5O_{15}$ for photocatalytic reduction of CO_2.[39] More recently, Dai reported the use of tungsten bronze structured $Ba_{0.5}Sr_{0.5}Nb_2O_6$ for piezoelectrically catalyzed hydrogen production.[40] Some researchers have reported the use of tungsten bronze structured materials in tribocatalysis for the degradation of dyes, including $Ba_4Nd_2Fe_2Nb_8O_{30}$,[41] $Ba_{1.4}Sr_{3.6}NdNb_7Ti_3O_{30}$,[42] and $Ba_{2.5}Sr_{2.5}Nb_8Ta_2O_{30}$.[43] These studies have demonstrated the remarkable catalytic potential of tungsten bronze structured materials in various catalysis processes, particularly tribocatalysis, but few researchers have previously reported the tribocatalytic generation of hydrogen using tungsten bronze structured ferroelectric materials.

In this work, tungsten bronze structured ferroelectric $Ba_{0.75}Sr_{0.25}Nb_{1.9}Ta_{0.1}O_6$ (BSNT) submicron powder was prepared through the conventional solid-state sintering method. Then, the BSNT submicron ferroelectric powder was used as the catalyst for tribocatalytic water splitting for hydrogen production and tribocatalytic degradation of RhB dye in wastewater. Under the friction stirring of three PTFE magnetic stir bars in pure water, the rate of hydrogen generation by the $Ba_{0.75}Sr_{0.25}Nb_{1.9}Ta_{0.1}O_6$ ferroelectric submicron powder is 200 μmol h^{-1} g^{-1}, and after 72 hours, the accumulated hydrogen production reaches 15 892.8 μmol g^{-1}. Additionally, this ferroelectric tungsten bronze ferroelectric material also exhibits excellent tribocatalytic degradation ability toward the RhB dye, with degradation efficiency reaching 96% in 2 hours. Through various characterization techniques, we have proposed a tribocatalyzed mechanism for this process, which involves the frictional separation of electron and hole pairs within the submicron powder, leading to the generation of hydroxyl and superoxide radicals in water for RhB degradation. Furthermore, the surface electrons of the particles were found to reduce free hydrogen ions in water, resulting in the production of hydrogen gas. The results presented in this study have significantly expanded the scope of potential applications for tungsten bronze structure-based materials in the field of tribocatalysis research.

2. Materials and methods

2.1 Preparation of BSNT submicron powder

The $Ba_{0.75}Sr_{0.25}Nb_{1.9}Ta_{0.1}O_6$ powder was prepared by the conventional solid-state sintering method. The starting materials used were $BaCO_3$ (99.99%, Aladdin), $SrCO_3$ (99.99%, Aladdin), Nb_2O_5 (99.99%, Sinopharm), and Ta_2O_5 (99.99%, Sinopharm). For a $BaCO_3 : SrCO_3 : Nb_2O_5 : Ta_2O_5$ molar ratio of 15 : 5 : 19 : 1, anhydrous ethanol was chosen as the milling medium. The mixture was subjected to ball milling for 6 hours, subsequently dried and compressed into a column, which was then subjected to a calcination process at 1000 °C for 4 hours. Later, the pre-sintered pellets were subjected to secondary ball milling. After ball milling, the dried powder was compressed into a column. Sintering was carried out in a high-temperature furnace at 1350 °C and under an air atmosphere for 6 hours. Finally, the ground powder was subjected to 12 hours of high energy ball milling at 300 rpm with ethanol as the grinding medium. Thus, the preparation of the BSNT submicron powder was completed.

2.2 Phase and structural characterization

The crystal structure of the BSNT powder was characterized by X-ray diffraction (Panalytical X'Pert Pro, The Netherlands). The surface structure and microscopic morphology of the powder were observed using field emission scanning electron microscopy (SEM, Hitachi S-4800, Japan), and the elemental composition and ratios of the powder were analyzed using an energy dispersive spectrometer (EDS, Horiba X-MAX, Japan). The particle size distribution of the BSNT powder was determined with a Zetasizer (Malvern Instruments ZS90, UK). The forbidden band widths of the powder were analyzed by ultraviolet-visible spectroscopy (UV-3600; Shimadzu, Kyoto, Japan).

2.3 Ferroelectric testing

BSNT ceramic tablets with a diameter of 8 mm and a thickness of 1 mm were synthesized at 1350 °C. Subsequently, the sample was polished on both sides, coated with silver paste, and then sintered at 650 °C for 30 minutes. Finally, the *P–E* hysteresis loops of the ceramic tablets were measured using a ferroelectric device (TF Analyzer 2000E; aixACCT, German) at a frequency of 10 Hz.

2.4 Catalytic hydrogen production performance testing

To investigate the tribocatalytic properties of BSNT, water was split by friction with particle powder to produce hydrogen. In this experiment, 0.1 g of BSNT submicron powder was added to 100 mL glassware containing 50 mL of deionized water and three PTFE magnetic stirring bars (∅ 8 mm × 55 mm), and no sacrificial agents such as methanol were used. The system was purged with air and filled with nitrogen to create a reaction atmosphere, thereby eliminating the impact of air on the reaction gases. The glassware was tightly sealed in a thermostatic water bath to maintain the catalytic reaction at approximately 25 °C. The sample was stirred in a dark environment at 500 rpm to eliminate the effects of temperature and illumination. The gas was regularly extracted from the glassware *via* a syringe and analyzed for hydrogen content using a gas chromatograph (GC9790II, Fuli Instruments, Zhejiang, China). For comparative experiments, 100 mg of the catalyst was precisely placed in a 100 mL airtight container, containing 50 ml of water. Piezoelectric catalysis was achieved using an ultrasonic

water bath generator operating at 40 kHz, and the reaction was carried out for 2 hours. Recurrent experiments involved withdrawing a specific quantity of gas from the system every 48 hours for analysis, after which the system was purged and fresh nitrogen gas was introduced.

2.5 Catalytic degradation performance testing

To evaluate the tribocatalytic properties of submicron particles, identical beakers and magnetic stirrers were employed for each experiment to eliminate the effects of stirring speed, rotational speed, and friction area on the results. To ensure consistency, all catalytic reactions were maintained at a constant temperature of approximately 25 °C and performed in a dark environment to minimize the impact of temperature and light on the results. For this experiment, 50 mg catalyst and 50 mL of rhodamine B solution (5 mg L^{-1}) were mixed in a glass beaker (∅ 51 mm × 70 mm). Three PTFE magnetic stirring bars (∅ 8 mm × 35 mm) were then used to stir the mixture. Finally, the supernatant was withdrawn at predetermined time intervals, and centrifuged with high-speed agitation. Then the liquid sample absorbance was measured using a UV-visible spectrophotometer to assess the degradation efficiency.

2.6 Active substance testing

The electron spin resonance spectroscopy (ESR) method, utilizing a Bruker A300 ESR instrument (Japan), is capable of detecting free radicals such as hydroxyl ($^{\bullet}OH$) and superoxide ($^{\bullet}O_2^-$) radicals. Radicals produced in solution can be analyzed using this technique. The experimental protocol specifically involved adding 100 mg of BSNT catalyst powder to 50 mL each of deionized water and methanol, followed by thorough mixing and stirring. Subsequently, 5,5-dimethyl-1-pyrroline-*N*-oxide (DMPO) was introduced as a capture agent at a concentration of 10 mg per 1 mL of solution. Under dark conditions, the PTFE-sealed magnetic bars were stirred at a speed of 500 rpm using friction. The solution was collected at regular intervals for the detection of ESR signals of radiation.

In a separate experiment, the effects of h^+, $^{\bullet}OH$ and $^{\bullet}O_2^-$ on the friction degradation properties were explored by adding different radical scavengers, such as 1 mM TBA (*tert*-butanol, hydroxyl radical scavenger), BQ (*p*-benzoquinone, superoxide radical scavenger) and EDTA[44] (ethylenediamine tetracarboxylic acid, cavity scavenger), respectively, and friction stirring under the same conditions as above.[45]

A fluorescence luminescence spectrophotometer (FL-FS5, Edinburgh, UK) was used to record the fluorescence spectrum resulting from the reaction of hydroxyl radicals with terephthalic acid (TA) to synthesize 2-hydroxyterephthalic acid (TAOH). This spectrophotometer can detect a distinctive photoluminescence signal at 425 nm upon excitation at 315 nm. This methodology was employed to ascertain whether $^{\bullet}OH$ is uniformly generated during the tribocatalysis process.[46]

2.7 Electrochemical testing

The Mott–Schottky curves of the samples were measured using an electrochemical workstation (Shanghai Chenhua CHI660), which was equipped with a standard three-electrode system. 10 mg of catalyst powder was mixed with 10 μL of 5% Nafion solution and 1 ml of anhydrous ethanol using ultrasonication. The resulting mixture was uniformly spread onto an ITO glass substrate (10 mm × 10 mm). To test the flat band potential of the catalyst, a sample coated with a working electrode, a Pt electrode, and a saturated calomel reference electrode were placed in a sodium sulfate solution.

3 Results and discussion

Fig. 1(a) shows the XRD pattern. The diffraction peaks were well indexed according to PDF #01-073-0126, and no evidence of a second phase was observed, suggesting that Ta^{5+} was successfully incorporated into the tungsten bronze lattice to form a solid solution with a pure phase of the tetragonal tungsten bronze structure.[47] The surface morphology of the BSNT ceramic after sintering is illustrated in Fig. 1(b). It is observed that the ceramic grains are well-grown with relatively uniform grain sizes, indicating favorable crystallization behavior during the sintering process. Fig. 1(c) presents the microscopic morphology of the material after high energy ball milling, indicating that it has a granular structure with irregularities in size and shape. The particle size distribution tested using a Zetasizer in Fig. 1(d) reveals an average particle size of 160 nm. The EDS mapping shown in Fig. 1(e) demonstrates that the BSNT ceramic elements are uniformly distributed with elemental contents of Ba (10.27%), Sr (3.26%), Nb (23.74%), Ta (1.26%), and O (61.48%), which is consistent with the design component ratio.

In tribocatalysis, the most important thing is the efficiency of the separation of electrons and holes. The tungsten bronze structured ferroelectric material exhibits a significant built-in electric field that affects tribocatalysis. Therefore, ferroelectric testing of the BSNT ceramic was conducted.[42] Fig. 1(f) shows the polarization–electric field (*P*–*E*) loop of the ceramic at a voltage of 700 V and a frequency of 10 Hz. The *P*–*E* loop reveals that the ceramic has a residual polarization intensity of 3.117 μC cm^{-2} and a maximum polarization intensity of 10.39 μC cm^{-2}. The results indicate that the ceramic samples exhibit good ferroelectricity at room temperature, fulfilling the requirement for the spontaneous polarization-induced built-in electric field in this application.

To verify the tribocatalytic effect, the powder was stirred using three PTFE magnetic stirring bars in deionized water. Subsequently, the gas generated inside the closed vessel was collected and introduced into a gas phase mass spectrometer. The amount of hydrogen generated during different stirring times was measured, as shown in Fig. 2(a)–(c). The hydrogen content increased with time and reached a maximum value of 15 892.8 μmol g^{-1} after 72 hours of stirring. The hydrogen production rates after different stirring times were compared, and the results showed that the rate remained approximately constant at 200 μmol h^{-1} g^{-1}. A satisfactory efficiency in tribocatalytic splitting of water was achieved.

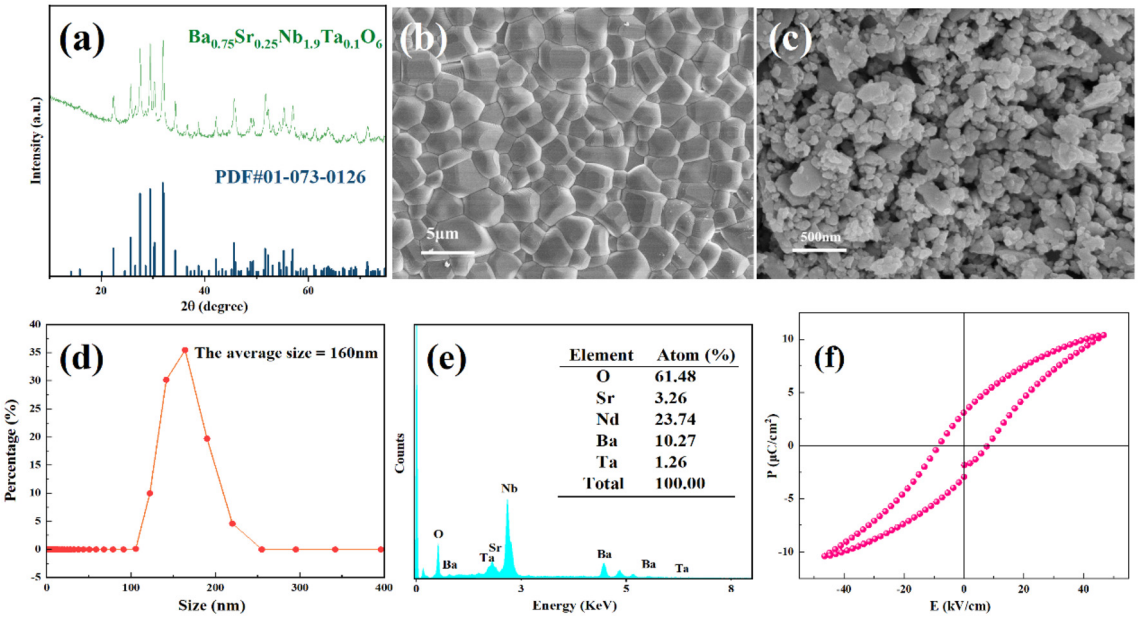

Fig. 1 (a) XRD diffraction pattern of the BSNT powder after high-energy ball milling, (b) SEM image of the BSNT ceramic, (c) SEM image of the BSNT powder after high-energy ball milling, (d) particle size distribution after high-energy ball milling, (e) EDS energy spectrum of BSNT, and (f) *P*–*E* loop of the BSNT ceramic measured at 700 V and 10 Hz at room temperature.

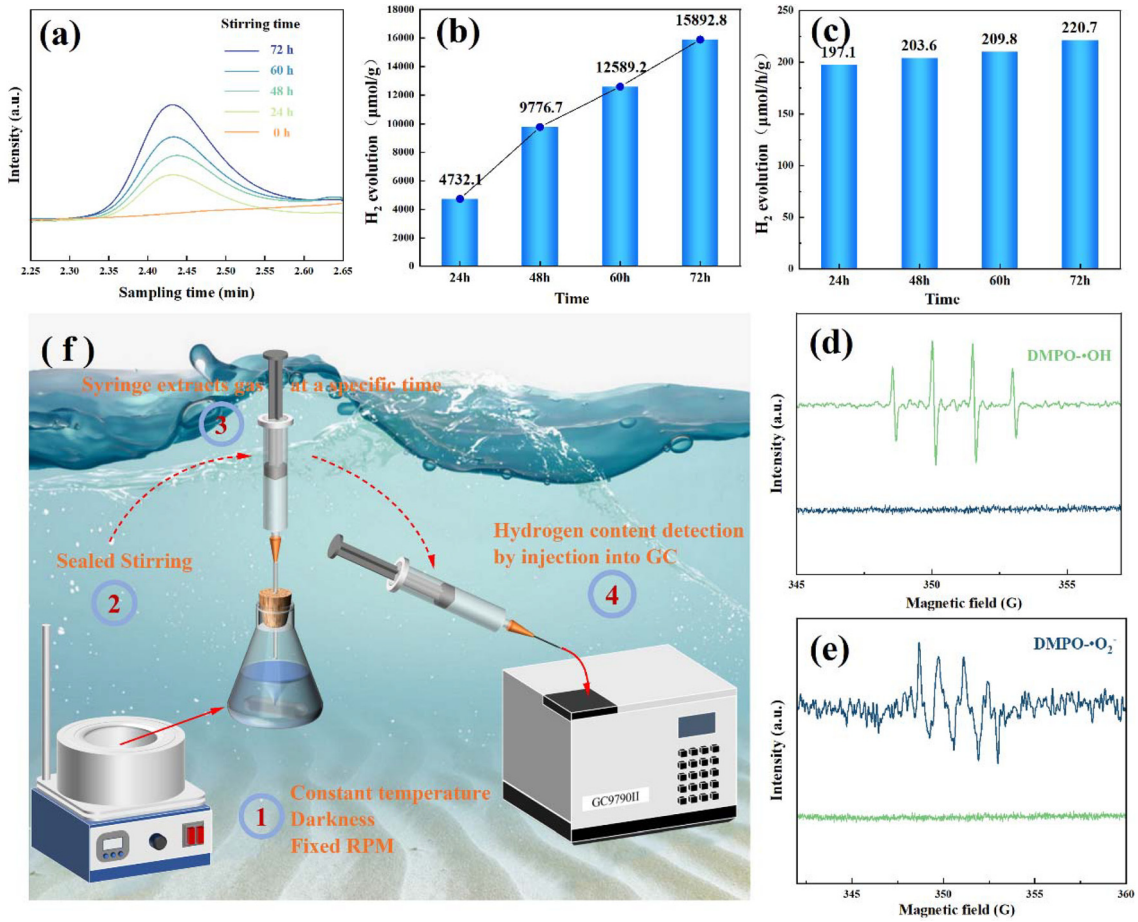

Fig. 2 (a) Hydrogen evolution chromatography (GC) spectra of BSNT under tribocatalytic conditions, (b) hydrogen production after different stirring times, (c) hydrogen production rate at different stirring times, and ESR spectra of DMPO spin trapping free radicals of BSNT, (d) DMPO–$^{\bullet}OH$ and (e) DMPO–$^{\bullet}O_2^-$. (f) Schematic diagram of the experimental setup and steps.

To further examine the generation of active substances during the tribocatalytic hydrogen production, electron spin resonance spectrometry (ESR) was employed to detect the presence of free radicals.[48] As illustrated in Fig. 2(d) and (e), there were no detectable signals for both compounds before the start of stirring. However, after stirring for 2 hours, DMPO–$^{\bullet}OH$ and DMPO–$^{\bullet}O_2^-$ peaks were observed, respectively. The generation of hydroxyl and superoxide radicals during the tribocatalysis process is a result of the production of electron and hole pairs.

To further verify that hydrogen production results from frictional catalysis during the PTFE stirring process, control experiments were conducted with one PTFE magnetic stirring bar and three PTFE magnetic stirring bars. The most important factor in the friction behavior is the magnitude of the friction force, and the frictional area produced by different numbers of stirring bars was investigated, as shown in Fig. 3(a). It was found that the hydrogen production rate for one PTFE stirring bar was 74.4 μmol h^{-1} g^{-1}, while that for three PTFE stirring bars was 203.6 μmol h^{-1} g^{-1}. These findings indicate that an increased frictional contact surface can prompt a greater amount of powder to participate in the catalytic reaction.[49]

The catalytic activity of the catalyst was examined under various experimental conditions, with the aim of ascertaining whether the observed catalytic behavior was a result of the frictional interaction between PTFE and the submicron powder of BSNT, as illustrated in Fig. 3(b). Under ultrasonic vibration conditions, no hydrogen production was observed in the closed vessel. Similarly, when the BSNT granular powder was stirred using a glass magnetic stirrer, no hydrogen production was observed. The compressive stress generated by the glass magnetic stirrer stirring in the glassware does not induce an observable catalytic reaction in BSNT, so hydrogen production can only occur under conditions of friction between a PTFE bar and BNST. These results exclude piezoelectric effects during catalytic water splitting of this work. However, in the case of stirring with three PTFE magnetic stirring bars without the addition of a catalyst, trace amounts of hydrogen were observed, which may be related to the catalysis from the friction between PTFE and glassware.[50]

To assess the stability of tribocatalytic splitting of water by the tungsten bronze structure, experiments were conducted. The BSNT granular powder was agitated with three glass magnetic stirrers in a closed container, and the gas generated within the system was sampled at 48-hour intervals for measurement. Subsequently, the system was evacuated to eliminate the influence of the gas produced during the previous 48 hours of reaction, and it was refilled with fresh nitrogen. This process was repeated three times, and the hydrogen content was measured for each cycle of experiment, as shown in Fig. 3(c). Notably, the hydrogen content produced remained within a specific range every 48 hours. Moreover, the XRD pattern of BSNT after the reaction exhibits a high degree of similarity to that of the previous reaction, as shown in Fig. 3(d), and the SEM micrograph of BSNT after the reaction also does not exhibit a different shape, as shown in Fig. 3(e). Finally, these results indicate the stability of the catalysis.

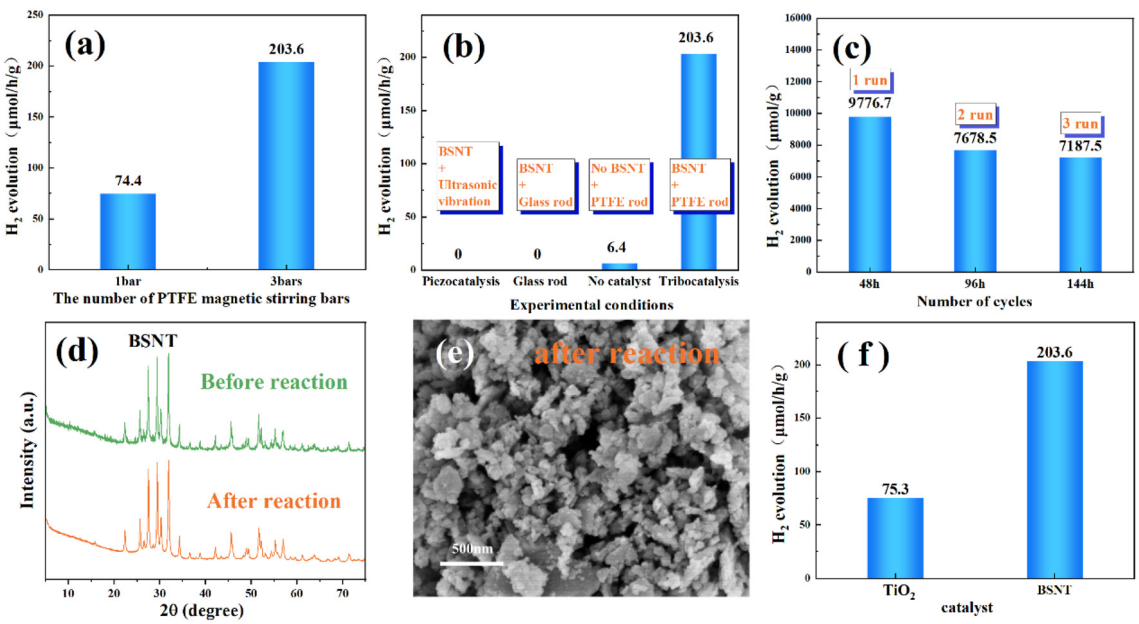

Fig. 3 (a) Effect of different numbers of magnetic bars on the hydrogen production rate. (b) Comparison of the hydrogen production rate under different experimental conditions (ultrasonic vibration, glass magnetic bar stirring, stirring with no catalyst added, and stirring with a catalyst added as normal). (c) Hydrogen production obtained from the experiments repeated three times with a measured cycle of 48 hours. (d) XRD patterns of the BSNT tribocatalyst before and after tribocatalysis. (e) SEM micrograph of the BSNT after 144 h tribocatalytic reaction. (f) Comparison of the tribocatalytic hydrogen production rates for TiO_2 and BSNT under the same experimental conditions.

The conventional TiO_2 photocatalyst has demonstrated remarkable potential in the field of tribocatalysis.[48] Previous experiments by Li *et al.* utilizing TiO_2 for catalyzing carbon dioxide reduction in friction resulted in hydrogen production of up to 0.75 ppm after 50 hours.[31] Therefore, the hydrogen production rates of BSNT and nano-TiO_2 (99.8%, 25 nm, Aladdin) were compared. As illustrated in Fig. 3(f), the rate of hydrogen production by BSNT was nearly three times as high as that by nano-TiO_2. It can be assumed that the built-in electric field of ferroelectric materials can promote the separation of electrons and holes, increase the number of surface charges, and enhance the efficiency of friction catalysis.[51] Finally, a comparison of different reports on tribocatalytic hydrogen production was made, as shown in Table 1, and the results suggest that BSNT has notable potential for tribocatalysed hydrogen production.

Table 1 Comparison of different reports on tribocatalytic hydrogen production

Catalysis	Magnetic stirring			
	Rotating part	Speed (r min^{-1})	Hydrogen production (μmol h^{-1})	Ref.
Co_3O_4 NiO	Teflon rod	1500	44.246	29
None	Copper disk	400	0.599	32
NiO	Teflon disk	400	2.394	46
Co_3O_4	Teflon disk	400	1.609	52
BSNT	Teflon rod	500	19.71	This work

To further assess the catalytic performance of BSNT, degradation experiments were conducted using the organic dye RhB. The catalytic powder (50 mg) was agitated with three PTFE magnetic stirring bars in a glass vessel containing the dye at a stirring speed of 500 rpm under dark conditions at room temperature. Fig. 4(a) illustrates the degradation diagram of BSNT on dyes and its degradation rate was calculated according to the following equation:

$$D = (1 - A/A_0) \times 100\%$$

where A_0 and A represent the initial and post-degradation absorption peak intensities of the solution, respectively, with RhB's characteristic absorption peak wavelength being 552 nm. It has been observed that the peak absorbance decreases as the stirring time increases. As shown in Fig. 4(a), the degradation efficiency of rhodamine B within 2 hours was

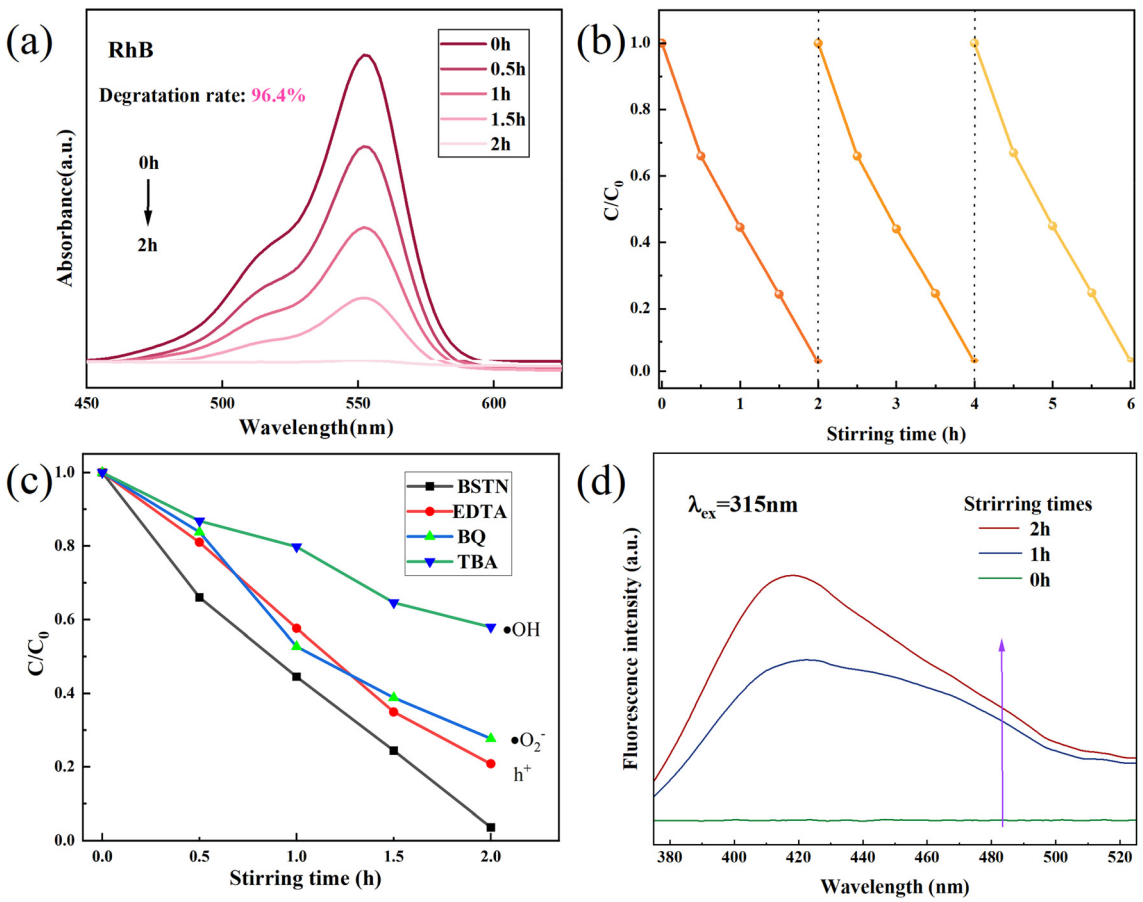

Fig. 4 (a) UV-Vis absorption spectra of BSNT in RhB dye solution at different times. (b) Cycling stability test of BSNT for degradation of RhB dye. (c) Effect of the addition of different radical scavengers on tribocatalysis. (d) ˙OH capture fluorescence spectra of suspensions containing BSNT and TA at 315 nm photoluminescence excitation wavelength.

96.4%. Comparative experiments demonstrated that degradation occurs solely during friction between PTFE and the catalyst, with the optimal energy consumption and degradation effect achieved at a rotation speed of 500 rpm. The experimental findings are presented in Fig. S1.† After a 2-hour reaction, the intermediates present in the solution were meticulously analyzed using liquid chromatography-mass spectrometry (LC-MS), enabling the deduction of potential degradation pathways (Fig. S2–3†). These intermediate products would ultimately be mineralized into H_2O and CO_2, indicating that BSNT also exhibits excellent tribocatalytic performance in degrading dyes.[45]

To assess the stability of the BSNT tribocatalyst in degradation of dyes, further experiments were conducted. After two hours of degradation, the catalyst was dried and recovered before being subjected to further degradation under identical conditions. As shown in Fig. 4(b), after three cycles of degradation, the efficiency of BSNT degradation could still exceed 94%, suggesting that BSNT possesses remarkable stability and recyclability.

We further elucidate the impact of free radicals generated during friction on dye degradation. As shown in Fig. 4(c), the addition of TBA radical trappers significantly reduced RhB degradation, and BQ also had a slight effect on the degradation efficiency, indicating that $^{\bullet}OH$ and $^{\bullet}O_2^-$ play crucial roles in the process, and that $^{\bullet}OH$ is the primary active degradation substance. As shown in Fig. 4(d), the fluorescence spectra indicate that the fluorescence intensity of 2-hydroxyterephthalic acid (captured $^{\bullet}OH$) was detected at a wavelength of 315 nm, which gradually increased with stirring time, confirming the appearance of $^{\bullet}OH$ radicals.

These above experimental results reveal that the submicron BSNT catalyst powder plays a crucial role in tribocatalysis. The catalytic behavior of BSNT is determined by its electronic band structure, which can be characterized through UV-visible spectroscopy and electrochemical testing. Therefore the bandgap of BSNT is calculated to be 3.29 eV utilizing the formula $(ah\nu)^{1/2} = A(h\nu - E_g)$, as depicted in Fig. 5(a).[53] And the bandgap of TiO_2 was determined to be 2.93 eV using the Tauc plot through the analysis of the obtained absorbance values in Fig. 5(b).[54]

The flat band energy (E_f) of BSNT was obtained by using an electrochemical workstation, as demonstrated in Fig. 5(c).

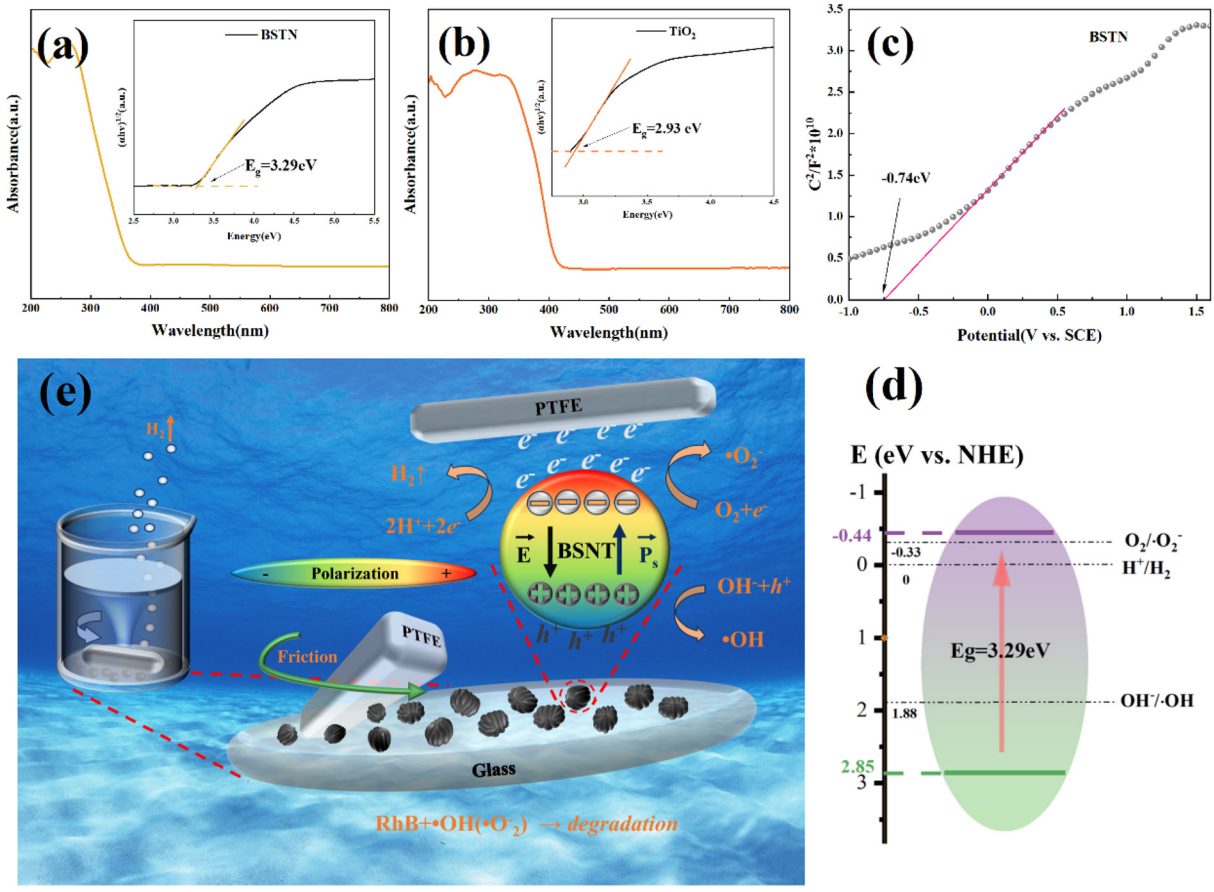

Fig. 5 (a) Band gap of BSNT submicron particles. (b) Band gap of nano-TiO_2. (c) Mott–Schottky plot of BSNT at 1 kHz. (d) Energy bands and potentials of $OH^-/^{\bullet}OH$, $O_2/^{\bullet}O_2^-$ and H^+/H_2 of BSNT. (e) Schematic representation of the tribocatalysis process.

Subsequently, the saturated calomel electrode (SCE) was converted to a standard hydrogen electrode (RHE) using the Nernst equation.[55]

$$E_{f(vs.\ RHE)} = E_{f(vs.\ SCE)} + 0.059 \times pH + E_{SCE}$$

The pH of the sodium sulfate electrolyte is 6.8, which resulted in an E_f value of −0.74 V *vs.* RHE (pH = 6.8) for the BSNT catalyst. The positive slope in the plot indicates that BSTN is an n-type semiconductor. For undoped n-type semiconductors, the E_f value is approximately 0.3 V more positive than the minimum value of the conduction band,[56] resulting in a value of −0.44 V *vs.* RHE for the conduction band of BSNT. Fig. 5(d) demonstrates that the position of the conduction band is thermodynamically optimal for water splitting to produce hydrogen, while also satisfying the requirements for generating hydroxyl and superoxide radicals.[57]

The energy band structure of nano-TiO_2 also meets the requirements for hydrogen production.[58] But with a similar bandgap, the hydrogen production efficiency of nano-TiO_2 is significantly lower than that of BSNT. Based on this, it can be inferred that ferroelectric built-in electrical fields have the potential to enhance tribocatalytic hydrogen production and dye degradation.

The built-in electric field of the BSNT ferroelectric material enhances the electron and hole separation during friction between the PTFE and the BSNT submicron powder.[42] As shown in Fig. 5(e), ferroelectric BSNTs have a depolarization field coming from bound charges as a result of spontaneous polarization. Positive and negative charges for space will be attracted to the particle surface to screen the bound charges. At equilibrium, the screening charges will generate an electric field that has the same intensity as the electric field from bound charges but in the reverse direction, leading to a net zero electric field in the particle. When friction occurs, the strong electrostatic attraction induced by friction drives electrons to migrate from the BSNT surface to the PTFE surface due to the difference in electron affinity between PTFE and BSNT. This will lead to a reduction in screening charges and disruption of the built-in electric field equilibrium inside the BSNT particles. Driven by this non-zero built-in electric field, the thermally excited electron–hole pairs will be quickly separated, the electrons in the conduction band (CB) will move to one end of the particle surface, and the holes will move to the other end of the particle surface. These electrons and holes will then trigger a series of redox reactions on the surface of the BSNT particles in sequence, in which the dissolved oxygen in water and the electrons are reduced to produce $^{\bullet}O_2^-$, and the OH^- is oxidized by holes to produce $^{\bullet}OH$; and finally, the dye is degraded. Hydrogen is generated by the direct reduction of hydrogen ions in water by electrons on the surface of the particles. Without the non-zero electric field due to electron transfer between BSNT and PTFE during friction, the separation of electron–hole pairs and their movement to the particle surface would be difficult. Based on the discussion and results described above, the possible mechanism can be explained using the following equations:[59]

$$BSNT \rightarrow BSNT + h^+_{VB} + e^-_{CB} \quad (1)$$

$$2H^+ + 2e^-_{CB} \rightarrow H_2 \uparrow \quad (2)$$

$$OH^- + h^+ \rightarrow {}^{\bullet}OH \quad (3)$$

$$O_2 + e^-_{CB} \rightarrow {}^{\bullet}O_2^- \quad (4)$$

$$RhB + {}^{\bullet}OH({}^{\bullet}O_2^-) \rightarrow \text{degradation} \quad (5)$$

4. Conclusion

The tungsten bronze structured $Ba_{0.75}Sr_{0.25}Nb_{1.9}Ta_{0.1}O_6$ ferroelectric submicron powder was studied and found to exhibit excellent performance in hydrogen production. Its tribocatalytic reaction produced 9776.7 μmol g^{-1} H_2 over a period of 48 hours, with a hydrogen production rate of approximately 200 μmol h^{-1} g^{-1}. In addition to its hydrogen production capabilities, the powder also showed remarkable potential for wastewater treatment through its ability to degrade the RhB dye, achieving a degradation efficiency of 96.4% within 2 hours of treatment. Through various characterization techniques, we have proposed a tribocatalytic mechanism for this process, which involves the frictional separation of electron and hole pairs within the submicron powder, leading to the generation of hydroxyl and superoxide radicals in water for RhB degradation. Furthermore, the surface electrons of the particles were found to reduce free hydrogen ions in water, resulting in the production of hydrogen gas. These findings demonstrate the significant potential of tungsten–bronze ferroelectrics for hydrogen production and wastewater treatment, and suggest that tribocatalysis could serve as a promising new approach for energy production and environmental remediation.

Conflicts of interest

There are no conflicts to declare.

Acknowledgements

The authors at the Guilin University of Technology thank the National Natural Science Foundation of China (12164012), the Science and Technology Plan of Guangxi (No. ZY22096019 and AA21238001), and the Science and Technology Plan of Guilin (ZY20220101) for financial support.

References

1 M. Zhang, Q. Hu, K. Ma, Y. Ding and C. Li, *Nano Energy*, 2020, **73**, 104810.

2 K. G. Motora and C.-M. Wu, *J. Taiwan Inst. Chem. Eng.*, 2020, **117**, 123–132.
3 X. Li and Q. Zhu, *EnergyChem*, 2020, **2**, 100033.
4 D. Xu, K. Li, B. Jia, W. Sun, W. Zhang, X. Liu and T. Ma, *Carbon Energy*, 2022, **5**, e230.
5 Z.-M. Wang, Q.-L. Hong, X.-H. Wang, H. Huang, Y. Chen and S.-N. Li, *Acta Phys.-Chim. Sin.*, 2023, 2303028.
6 H. Ishaq, I. Dincer and C. Crawford, *Int. J. Hydrogen Energy*, 2022, **47**, 26238–26264.
7 D. Liu, L. Feng, L. Cao, T. Xiao and J. Huang, *J. Alloys Compd.*, 2022, **890**, 161920.
8 T. Rin, C. Sangwichien, R. Yamsaengsung and T. Reungpeerakul, *Int. J. Hydrogen Energy*, 2021, **46**, 28450–28461.
9 A. Shi, H. Li, S. Yin, Z. Hou, J. Rong, J. Zhang and Y. Wang, *Appl. Catal., B*, 2018, **235**, 197–206.
10 M. Zhang, F. Xie, L. Zhang, X. Jian, J. Liu, X. Zhang, Y. Wang, R. Li and C. Fan, *Mater. Lett.*, 2022, **321**, 132416.
11 K. G. Motora, C.-M. Wu, T. F. Chala, M.-H. Chou, C.-F. J. Kuo and P. Koinkar, *Appl. Surf. Sci.*, 2020, **512**, 145618.
12 Y. Long, H. Xu, J. He, C. Li and M. Zhu, *Surf. Interfaces*, 2022, **31**, 102056.
13 Y. Du, T. Lu, X. Li, Y. Liu, W. Sun, S. Zhang and Z. Cheng, *Nano Energy*, 2022, **104**, 107919.
14 R. Belitz, P. Meisner, M. Coeler, U. Wunderwald, J. Friedrich, J. Zosel, M. Schelter, S. Jachalke and E. Mehner, *Energy Harvesting and Systems*, 2017, **4**, 107–113.
15 X. Gao, J. Qi, S. Wan, W. Zhang, Q. Wang and R. Cao, *Small*, 2018, **14**, 1803361.
16 X. Xu, S. Chen, Z. Wu, Y. Jia, L. Xiao and Y. Liu, *Nano Energy*, 2018, **50**, 581–588.
17 B. Yang, H. Chen, Y. Yang, L. Wang, J. Bian, Q. Liu and X. Lou, *Chem. Eng. J.*, 2021, **416**, 128986.
18 Y. Liu, K. Zhang, D. Zhang, W. Dong, T. Jiang, H. Zhou, L. Li and B. Mao, *J. Energy Storage*, 2021, **41**, 102844.
19 F Fan, Z. Tian and Z. Wang, *Nano Energy*, 2012, **1**, 328–334.
20 C. Kajdas, A. Kulczycki and D. Ozimina, *Tribol. Int.*, 2017, **107**, 144–151.
21 K. G. Motora, C. M. Wu, C. R. M. Jose and G. M. Rani, *Advanced Functional Materials*, 2024, 2315069, DOI: **10.1002/adfm.202315069**.
22 P. Li, J. Wu, Z. Wu, Y. Jia, J. Ma, W. Chen, L. Zhang, J. Yang and Y. Liu, *Nano Energy*, 2019, **63**, 103832.
23 M. Wu, H. Lei, J. Chen and X. Dong, *J. Colloid Interface Sci.*, 2021, **587**, 883–890.
24 Y. Xu, R. Yin, Y. Zhang, B. Zhou, P. Sun and X. Dong, *Langmuir*, 2022, **38**, 14153–14161.
25 X. Li, W. Tong, W. Song, J. Shi and Y. Zhang, *J. Cleaner Prod.*, 2023, **414**, 137566.
26 M. Vásquez-Rendón, M. Romero-Sáez, J. Mena, V. Fuenzalida, I. Berlanga and M. L. Álvarez-Láinez, *Polym. Adv. Technol.*, 2020, **32**, 1615–1625.
27 C. Georgescu, L. Deleanu, L. C. Titire and A. C. Ceoromila, *Materials*, 2021, **14**, 997.
28 G. Hitoki, T. Takata, S. Ikeda, M. Hara, J. N. Kondo, M. Kakihana and K. Domen, *Catal. Today*, 2000, **63**, 175–181.
29 S. Ikeda, T. Takata, M. Komoda, M. Hara, J. N. Kondo, K. Domen, A. Tanaka, H. Hosono and H. Kawazoe, *Phys. Chem. Chem. Phys.*, 1999, **18**, 4485–4491.
30 S. Ikeda, T. Takata, T. Kondo, G. Hitoki, M. Hara, J. N. Kondo, K. Domen, H. Hosono, H. Kawazoe and A. Tanaka, *Chem. Commun.*, 1998, 2185–2186, DOI: **10.1039/A804549F**.
31 P. Li, C. Tang, X. Xiao, Y. Jia and W. Chen, *Friction*, 2021, **10**, 1127–1133.
32 X. Cui, H. Wang, H. Lei, X. Jia, Y. Jiang, L. Fei, Y. Jia and W. Chen, *ChemistrySelect*, 2023, **8**, e202204146.
33 X.-J. He, L. Li, Z.-S. Xie, Y.-C. Zhang, J. Zhang, Z.-B. Gu, H. Zhang, G. Yuan and S.-T. Zhang, *J. Eur. Ceram. Soc.*, 2021, **41**, 2435–2442.
34 X. Li, Y. Du, L. Ge, C. Hao, Y. Bai, Z. Fu, Y. Lu and Z. Cheng, *Adv. Funct. Mater.*, 2022, **33**, 2210194.
35 Z. J. Yang, X. Q. Liu, X. L. Zhu and X. M. Chen, *Appl. Phys. Lett.*, 2020, **117**, 122902.
36 D. Fan, R. Chong, F. Fan, X. Wang, C. Li and Z. Feng, *Chin. J. Catal.*, 2016, **37**, 1257–1262.
37 K. Shimizu, H. Kato, M. Kobayashi and M. Kakihana, *Appl. Catal., B*, 2017, **206**, 444–448.
38 J. Wang, C. Xiao, X. Wu and G. Zhang, *Chin. J. Chem.*, 2017, **35**, 189–195.
39 S. Yoshizawa, Z. Huang, K. Teramura, H. Asakura, S. Hosokawa and T. Tanaka, *ACS Appl. Mater. Interfaces*, 2019, **11**, 37875–37884.
40 J. Dai, N. Shao, S. Zhang, Z. Zhao, Y. Long, S. Zhao, S. Li, C. Zhao, Z. Zhang and W. Liu, *ACS Appl. Mater. Interfaces*, 2021, **13**, 7259–7267.
41 C. Sun, X. Guo, R. Ji, C. Hu, L. Liu, L. Fang, Z. Cheng and N. Luo, *Ceram. Int.*, 2021, **47**, 5038–5043.
42 Z. Jin, X. Zheng, Z. Zhu, C. Hu, L. Liu, L. Fang, N. Luo and Z. Cheng, *Mater. Today Chem.*, 2023, **29**, 101427.
43 C. Sun, X. Guo, C. Hu, L. Liu, L. Fang, Z. Cheng and N. Luo, *RSC Adv.*, 2021, **11**, 13386–13395.
44 J. Cao, Y. Jia, X. Wan, B. Li, Y. Zhang, S. Huang, H. Yang, G. Yuan, G. Li, X. Cui and Z. Wu, *Ceram. Int.*, 2022, **48**, 9651–9657.
45 Z. Jin, X. Zheng, Z. Zhu, C. Hu, L. Liu, L. Fang and Z. Cheng, *Appl. Surf. Sci.*, 2023, **625**, 157228.
46 H. Lei, X. Jia, H. Wang, X. Cui, Y. Jia, L. Fei and W. Chen, *Coatings*, 2023, **13**, 396.
47 Z. Yang, R. Gu, L. Wei and H. Ren, *J. Alloys Compd.*, 2010, **504**, 211–216.
48 X. Cui, P. Li, H. Lei, C. Tu, D. Wang, Z. Wang and W. Chen, *Sep. Purif. Technol.*, 2022, **289**, 120814.
49 Q. Zhang, Y. Jia, X. Wang, L. Zhang, G. Yuan and Z. Wu, *Sep. Purif. Technol.*, 2023, **307**, 122846.
50 S. Zhang, H. Yu, X. Zhu, X. Sang, Y. Li, J. Fu, Q. Li, Y. Zhang and W. Ye, *ACS Appl. Polym. Mater.*, 2023, **5**, 3585–3594.
51 Q. Tang, M. Zhu, H. Zhang, J. Gao, K. W. Kwok, L.-B. Kong, Y. Jia, L. Liu and B. Peng, *Nano Energy*, 2022, **100**, 107519.

52 X. Jia, H. Wang, H. Lei, C. Mao, X. Cui, Y. Liu, Y. Jia, W. Yao and W. Chen, *J. Adv. Ceram.*, 2023, **12**, 1833–1843.
53 A. Zhanga, Z. Liua, B. Xiea, J. Lua, K. Guoa, S. Keb, L. Shub and H. Fan, *Appl. Catal., B*, 2020, **279**, 119353.
54 A. Raja, N. Son, M. Swaminathan and M. Kang, *J. Cleaner Prod.*, 2023, **423**, 138809.
55 Y. Li, W. Zhou, H. Wang, L. Xie, Y. Liang, F. Wei, J.-C. Idrobo, S. J. Pennycook and H. Dai, *Nat. Nanotechnol.*, 2012, **7**, 394–400.
56 W. Yin, L. Bai, Y. Zhu, S. Zhong, L. Zhao, Z. Li and S. Bai, *ACS Appl. Mater. Interfaces*, 2016, **8**, 23133–23142.
57 Y. Sun, X. Li, A. Vijayakumar, H. Liu, C. Wang, S. Zhang, Z. Fu, Y. Lu and Z. Cheng, *ACS Appl. Mater. Interfaces*, 2021, **13**, 11050–11057.
58 X. Du, J. Hu, A. Liu and Y. Cao, *J. Colloid Interface Sci.*, 2021, **588**, 670–679.
59 X. Li, W. Tong, J. Shi, Y. Chen, Y. Zhang and Q. An, *J. Mater. Chem. A*, 2023, **11**, 4458–4472.